

# Numerical Investigation of Flow Inside the Collector of a Solar Chimney Power Plant

M. K. Hasan\* and A. Gross<sup>†</sup>

New Mexico State University, Las Cruces, NM 88003

L. Bahrainirad<sup>‡</sup> and H.F. Fasel<sup>§</sup>

University of Arizona, Tucson, AZ 85721

The flow through the collector of a solar chimney power plant model on the roof of the Aerospace and Mechanical Engineering building at the University of Arizona was investigated numerically for the conditions of the experiment. The measured wall temperature and inflow velocity for a representative day were chosen for the simulation. The simulation was performed with a newly developed higher-order-accurate compact finite difference code. The code employs fifth-order-accurate biased compact finite differences for the convective terms and fourth-order-accurate central compact finite differences for the viscous terms. A fourth-order-accurate Runge-Kutta method was employed for time integration. Unsteady random disturbances are introduced at the inflow boundary and the downstream evolution of the resulting waves was investigated based on the Fourier transforms of the unsteady flow data. Steady azimuthal waves with a wavenumber of roughly four based on the channel half-height are the most amplified as a result of Rayleigh-Bénard-Poiseuille instability. Different from plane Rayleigh-Bénard-Poiseuille flow, these waves appear to merge in the streamwise direction. Oblique waves are also amplified. The growth rates are however lower than for the steady modes. Because of the strong streamwise flow acceleration, the growth rates decrease in the downstream direction.

#### I. Introduction

The solar chimney power plant (SCPP) represents a sustainable energy pathway from solar irradiation to electrical energy. The collector, turbine and chimney are the three major components of SCPPs. The air inside the collector is heated by the solar radiation and accelerates towards the collector center, where it passes through turbines and then escapes through the central chimney. The first solar chimney power plant was designed by Schlaich, Bergermann and Partner in Manzanares, Spain. It was operated between 1982 to 1989 and produced approximately 50kW of electrical power.<sup>1–4</sup> According to Schlaich, an estimate for the electrical power can be obtained from

$$P = \eta_c \eta_t \frac{2}{3} g \frac{H_t \pi r_{coll}^2 I}{c_p T_a} \,, \tag{1}$$

where  $\eta_c$  and  $\eta_t$  are the collector and turbine efficiency, g is the gravitational acceleration, I is the solar irradiation, and  $T_a$  is the ambient temperature. Different from concentrated and photovoltaic solar power plants, the generated power scales with the collector area,  $\pi r_{coll}^2$  and the chimney height,  $H_{ch}$ .

The radial channel flow between two horizontal parallel plates with temperature gradient in the wall-normal direction and opposing gravitational field is known as radial Rayleigh-Bénard-Poiseuille (RBP) flow. Radial RBP flows as found for example in the collector of a SCPP, can exhibit buoyancy-driven instability. The onset of flow instability is governed by two dimensionless numbers which are the Reynolds number,

$$Re = \frac{u_{max}h/2}{\nu},\tag{2}$$

<sup>\*</sup>Graduate Research Assistant, Member AIAA.

<sup>&</sup>lt;sup>†</sup>Assistant Professor. Associate Fellow AIAA.

<sup>&</sup>lt;sup>‡</sup>Graduate Research Assistant, Member AIAA

<sup>§</sup>Professor. Fellow AIAA.

with maximum velocity,  $u_{max}$ , channel height, h, and kinematic viscosity,  $\nu$ , and the Rayleigh number,

$$Ra = \frac{gh^3\gamma\Delta T}{\nu\alpha}\,, (3)$$

with volumetric thermal expansion coefficient,  $\gamma$ , temperature difference,  $\Delta T$ , and thermal diffusivity,  $\alpha$ . The buoyancy-driven instability of plane RBP flows has been investigated in detail in the past. Linear stability investigations of plane RBP flow by Gage and Reid<sup>5</sup> provided neutral curves for the onset of both buoyancy and viscosity-driven instability. For  $Re < Re_c = 5,400$  and  $Ra > Ra_c = 1,708$ , plane RBP flow exhibits buoyancy-driven instability and the most unstable modes are three-dimensional (3-D) and have a wave angle of 90 degrees. When the Reynolds number is greater than  $Re_c = 5400$  and the Rayleigh number is less than  $Ra_c = 1708$ , viscosity-driven instability occurs and two-dimensional (2-D) Tollmien-Schlichting (T-S) waves with a wave angle of 0 degree are the most amplified. The results by Gage and Reid<sup>5</sup> were confirmed by numerous numerical and experimental studies. A linear stability theory (LST) analysis by Pearlstein<sup>6</sup> showed that the most critical disturbances for RBP flow are either 2-D transverse or longitudinal modes. Chang et al.<sup>7,8</sup> investigated plane RBP flow experimentally and found that the flow structures first developed near the channel side walls. For a channel with finite rectangular cross section, transverse rolls appeared first at a low Reynolds number.<sup>9,10</sup> However, 3-D longitudinal rolls developed when the Reynolds number was increased.

The hydrodynamic instability of radial RBP flows, of particular relevance for the design and operation of SCPPs at the critical Reynolds and Rayleigh number for the instability to occur, has attracted comparatively little attention. Because of continuity ( $\rho v \propto 1/r$ -relationship), the collector flow is accelerated in the streamwise (radial) direction. Also different from plane RBP flow, where the channel maintains a constant aspect ratio and there is no limitation on the transverse wavenumbers, for radial channel flow the transverse wavelength has to be an integer fraction of the circumference. Moreover, since acceleration generally has a stabilizing effect, 11 the stability characteristics of inward radial RBP flow are likely different from those of plane RBP flow. Bernardes et al. 12 numerically investigated various thermo-hydrodynamic properties, such as the temperature fields, and mass flow rate for different geometric configurations of SCPPs. Reynolds-averaged Navier-Stokes (RANS) calculations by Pastohr et al. 13 revealed that the mass flow rate and pressure difference across the collector had a strong affect on the efficiency of SCPPs. Xu et al. 14 investigated numerically how the generated power and energy losses of the SCPP system are affected by the solar radiation and turbine efficiency. Based on their analysis, the large mass flow rate through the chimney is one of the primary reasons for the energy losses. The influence of the chimney geometry (such as area ratio between chimney inlet and outlet and divergence angle) on the power output was investigated numerically by Hu et al. 15 The SCPP power output was found to be higher for divergent chimneys than for conventional cylindrical chimneys. Despite the large volume of literature concerned with the more practical aspects of SCPP design, scientific literature on the hydrodynamic instability of radial RBP flows is very rare.

A numerical investigation of the radial outward RBP flow between two circular plates was carried out by Van Santen et al.  $^{16,17}$  Their research suggests that streamwise waves are the most unstable at low Reynolds numbers (10 to 50 with Ra = 2000) which opposes the results by Gage and Reid<sup>5</sup> according to which 2-D waves should be stable for this Reynolds number range. Fasel et al.  $^{18,19}$  carried out large-eddy simulations for the collector of a 1:33 scale model of the Manzanares SCPP. Both transverse (close to the inlet) and longitudinal rolls (close to the outlet) were observed in the simulations. Recently, Ladan et al.  $^{20}$  carried out an experimental investigation of the flow inside the collector of a 1:33 model of the Manzanares SCPP. Thermocouple temperature measurements as well as hotwire anemometer velocity measurements provided a good characterization of the flow in the collector and the wall and collector cover temperatures. However, because of technical difficulties and the unavoidable freestream noise associated with uncontrolled outdoor experiments, flow structures inside the collector arising from inherent instabilities were not investigated. This backdrop provides the motivation for the present numerical analysis of the flow through the collector of the scaled model.

This paper reports on numerical stability investigations of the flow inside the collector of the 1:33 scale SCPP model at the University of Arizona. The inflow temperature and bulk velocity as well as the ground and collector cover temperatures were matched to measurements by Ladan et al.<sup>20</sup> for a representative day. The numerical stability analysis was carried out with a new higher-order-accurate compact finite difference code. First, the governing equations, discretization, and boundary conditions are described. Next, the setup of a spatial stability simulation for a specific combination of Reynolds and Rayleigh number that is representative of the experiment is discussed. The simulation data were Fourier transformed to analyze the

growth rates, wave angles, and phase speeds of the disturbance waves. The paper concludes with a brief discussion of the results.

# II. Methodology

#### A. Governing Equations

The compressible Navier-Stokes equations in cylindrical coordinates<sup>21</sup>

$$\frac{\partial \mathbf{Q}}{\partial t} + \frac{\partial \mathbf{A}}{\partial z} + \frac{\partial \mathbf{B}}{\partial r} + \frac{1}{r} \frac{\partial \mathbf{C}}{\partial \theta} + \frac{1}{r} \mathbf{D} = \mathbf{H}, \tag{4}$$

with state vector,  $\mathbf{Q}$ , flux vectors,  $\mathbf{A}$ ,  $\mathbf{B}$ ,  $\mathbf{C}$ , and source term vectors  $\mathbf{D}$  and  $\mathbf{H}$  were solved numerically. The state vector is

$$\mathbf{Q} = \left[ \rho, \rho u, \rho v, \rho w, \rho e \right]^T, \tag{5}$$

where u, v, and w are the velocities in the wall-normal (z), radial (r), and azimuthal  $(\theta)$  direction. The total energy is defined as  $e = \epsilon + 1/2(u^2 + v^2 + w^2)$ , with internal energy,  $\epsilon = c_v T$ , where T is the temperature and  $c_v$  is the specific heat at constant volume. A reference velocity,  $u_{ref} = u_{max}$ , reference length scale,  $L_{ref}$ , reference temperature,  $T_{ref}$ , and reference density,  $\rho_{ref}$ , were used to non-dimensionalize the governing equations. Here,  $u_{max}$  is the channel maximum velocity at the inflow and h is the channel height. The pressure is calculated from the ideal gas equation,

$$p = \rho RT, \tag{6}$$

with gas constant, R, and, non-dimensionalized by  $\rho_{ref}u_{ref}^2$ . The reference Mach number was set to M=0.025. More details on the governing equations can be found in Hasan and Gross.<sup>22,23</sup>

#### B. Computational Domain and Discretization

A "pizza-slice" shaped computational domain was employed for the present direct numerical simulation (DNS) of the flow through the collector of the 1:33 scale SCPP model at the University of Arizona (Fig. 1). With the chosen non-dimensionalization, the collector inflow radius is  $r_2 = 125$  and the outflow radius is  $r_1 = 10$ . A coordinate transformation which clusters grid points near the top and bottom wall was employed in the wall-normal direction. A total of J grid points were distributed in the wall-normal direction,

$$z_j = \left[ \frac{\tan^{-1}(jc - f_1)}{f_2} + 1 \right] \times \frac{h}{2}, \tag{7}$$

where J = 64 is the total number of grid points in the wall-normal direction,  $f_1 = Jc^*/2$  and  $f_2 = \tan^{-1}(f_1)$ ,  $c^* = 0.05$  is a user-specified constant, and j is the grid line index. An equidistant grid point distribution was employed in the streamwise direction and a total of 512 points were used. The grid opening angle was set to 7.5 degrees.

Fifth-order-accurate upwind-biased and downwind-biased compact finite differences<sup>24</sup> were utilized for discretizing the convective terms in the wall-normal and radial direction. Fourth-order-accurate compact finite differences for non-equidistant meshes by Shukla et al.<sup>25</sup> were employed for discretizing the viscous terms. Fast Fourier transforms were used to calculate the derivatives in the azimuthal direction. A fourth-order-accurate explicit low-storage Runge-Kutta method<sup>26</sup> was employed for time integration.

#### C. Boundary Conditions

In the azimuthal direction, periodic boundary conditions were implicitly enforced by the Fourier-based spectral discretization. No-slip and no-penetration as well as isothermal boundary conditions were employed at both walls. The bottom,  $T_b$ , and top wall,  $T_t$ , temperature were held constant. When the viscous terms are neglected, the wall-normal pressure gradient at the walls depends only on the buoyancy term,

$$\frac{\partial p}{\partial z} = g(1 - \rho). \tag{8}$$

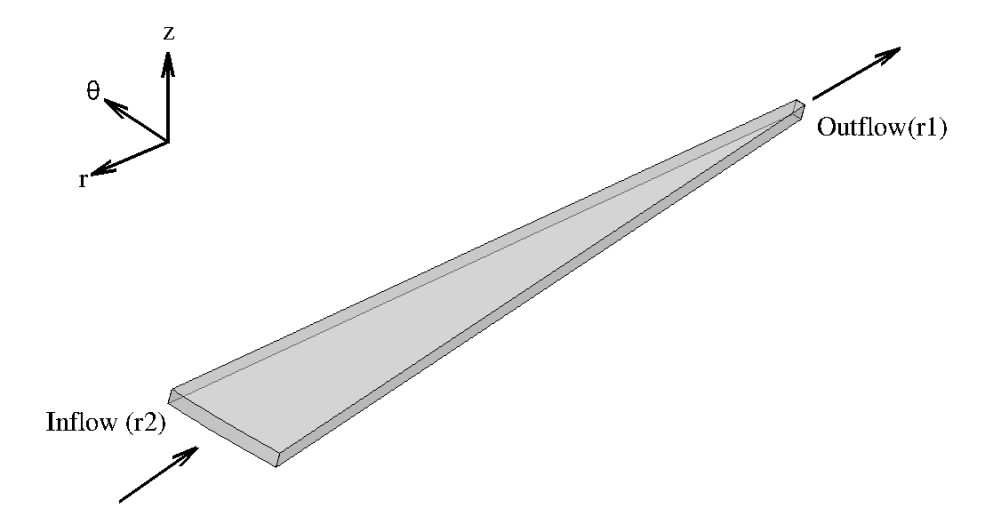


Figure 1. Computational domain.

The  $\partial p/\partial z$  derivative was computed with a fourth-order-accurate one-sided finite difference stencil. The bottom and top wall pressure are obtained from,

$$p_0 = \frac{-12g\frac{\partial z}{\partial \eta} + 48p_1 - 36p_2 + 16p_3 - 3p_4}{25 - \frac{12g}{RT_0}\frac{\partial z}{\partial \eta}},$$
(9)

and

$$p_J = \frac{12g\frac{\partial z}{\partial \eta} + 48p_{J-1} - 36p_{J-2} + 16p_{J-3} - 3p_{J-4}}{25 + \frac{12g}{RT_J}\frac{\partial z}{\partial \eta}} \ . \tag{10}$$

A non-reflecting boundary condition based on Riemann invariants<sup>27</sup> was employed at the inflow boundary. At the outflow boundary, a characteristics-based boundary condition by Gross and Fasel<sup>28</sup> was applied. Both boundary conditions require reference profiles. The reference profiles were obtained by solving the equations describing one-dimensional laminar plane RBP flow.<sup>22, 23</sup>

## D. Linear Stability Analysis

According to what is customary in linear stability theory (LST), a wave ansatz of the form

$$u'(r, z, \theta, t) = \sum \hat{u}(z)e^{i(\alpha r + \beta \theta - \omega t)}, \qquad (11)$$

is made for the disturbance waves where  $\alpha = \alpha_r + i\alpha_i$  is the streamwise (radial) wavenumber,  $\beta$  is the spanwise (azimutal) wavenumber, and  $\omega$  is the angular frequency. Here,  $\hat{u}(z)$  are the eigenfunctions. The real part of the streamwise,  $\alpha_r$ , and the spanwise wavenumber,  $\beta$ , are related to the wavelength via  $\alpha_r = 2\pi/\lambda_r$  and  $\beta = 2\pi/\lambda_\theta$ . The angular frequency is related to the period via  $\omega = 2\pi/T$ . In this paper the modes are referenced by their temporal, n, and spanwise or azimuthal mode number, k. Spatial disturbance growth occurs for  $\alpha_i < 0$ .

The data obtained from the simulations were Fourier transformed in the azimuthal direction and in time. For example, the disturbance velocity at a given location is described by,

$$u'(r,z,\theta,t) = \hat{a}_{cc}(r,z)\cos\omega t\cos\beta r\theta + \hat{a}_{cs}(r,z)\cos\omega t\sin\beta r\theta + \hat{a}_{sc}(r,z)\sin\omega t\cos\beta r\theta + \hat{a}_{ss}(r,z)\sin\omega t\sin\beta r\theta.$$
(12)

The amplitude (A) and phase  $(\psi)$  of the right and left traveling waves are computed from these Fourier coefficients and the spatial growth rate is

$$\alpha_i = -\frac{\partial \ln A}{\partial s} \,, \tag{13}$$

where  $s = r_2 - r$  is the stremwise coordinate. The phase speed is obtained from  $c = \omega/K$  with  $K = \sqrt{\alpha_r^2 + \beta^2}$ , and the wave angle is given by  $\phi = tan^{-1}(\beta/\alpha_r)$ . The growth rates, phase speeds, and wave angles were computed from the wall-normal velocity at the channel mid-height. Additional details are provided in Hasan and Gross.<sup>22,23</sup>

## III. Results

### A. Brief Review of Experimental Results and Calculation of Simulation Parameters

The experiments by Ladan et al.<sup>20</sup> provide the foundation for the present numerical analysis of the solar chimney power plant collector. In this section first a brief description of the exerimental set-up and results is provided. Then the calculation of the different parameters required for the set-up of the simulation is investigated. Figure 2a shows the solar chimney power plant model on the roof of the Aerospace and Mechanical Engineering Department at the University of Arizona. Figure 2b displays the instrumented section of the collector. The radius of the collector inlet and outlet (chimney inlet) is  $r_{coll} = 4.1m$  and  $r_{ch} = 0.15m$ , respectively, and the chimney height is  $H_{ch} = 5.9m$ . The collector panels are at a distance of h = 6.6cm from the ground. Eight thermocouples (four near the collector panels and four at the ground) were placed at different radial locations. The corresponding radial locations are shown in Fig. 2c. The time-averaged temperatures at four radial locations are plotted in Fig. 3a. Overall the temperature at the ground and near the cover is increasing as the flow travels towards the collector outlet. Figure 3b exhibits the radial velocity at the corresponding four locations inside the collector. The velocity inside the collector increases in the radial direction according to the radial continuity equations with location 1 having the highest velocity. More details on the experiment can be found in Ladan et al.<sup>20</sup>

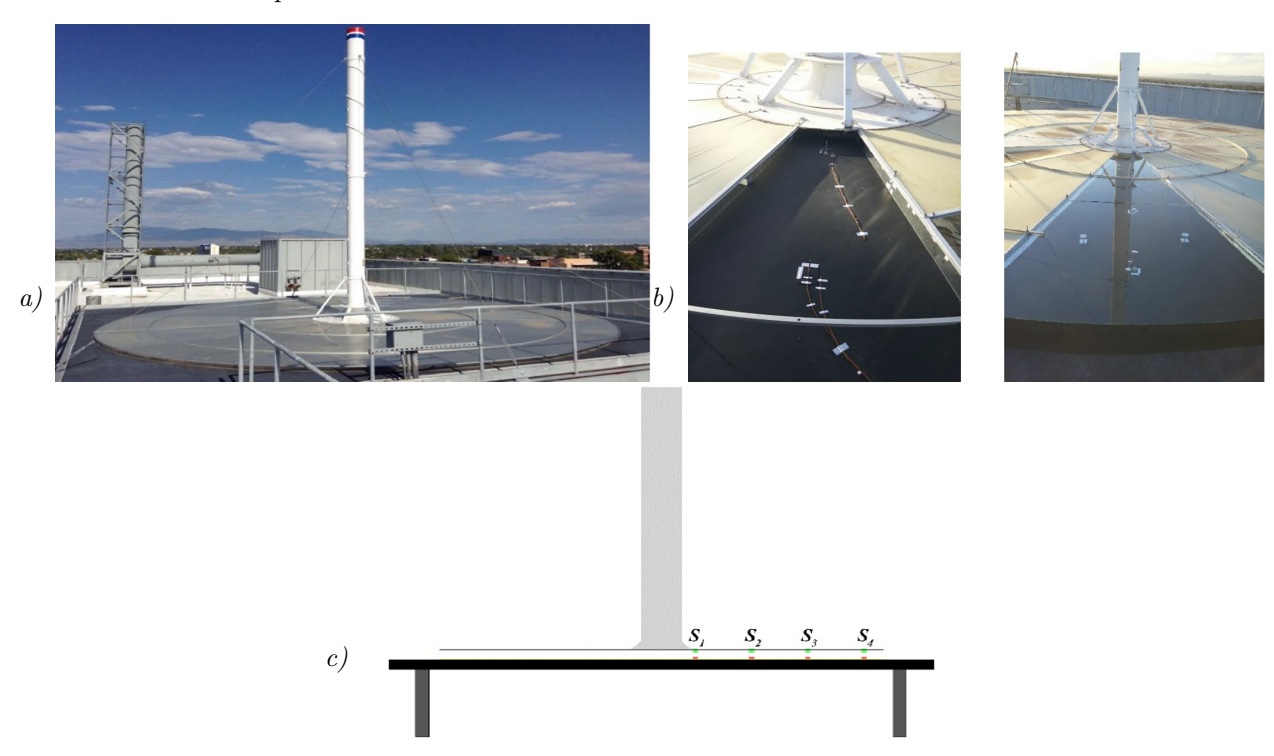


Figure 2. a) Solar chimney power plant model at the University of Arizona, b) instrumented section of the collector, and c) schematic side view of the model with thermocouples in position 1, 2, 3 and 4 (Figures reproduced from Ladan et al.  $^{20}$ )

The collector half-height was taken as the reference length scale,  $L_{ref} = h/2 = 0.033m$ . Based on this length scale, the inflow radius of the collector becomes  $r_1 = 124.24 \approx 125$ . An outflow radius of  $r_2 = 10$  was chosen for the simulation which gives an outflow radius of approximately 0.3m. Based on the experimental data, it was decided to choose a bottom wall temperature of  $T_b = 75^{\circ}C = 348.15K$ , a top wall (collector cover) temperature of  $T_t = 60^{\circ}C = 333.15K$ , and an ambient temperature of  $T_a = T_{ref} = 38.4^{\circ}C = 1000$ 

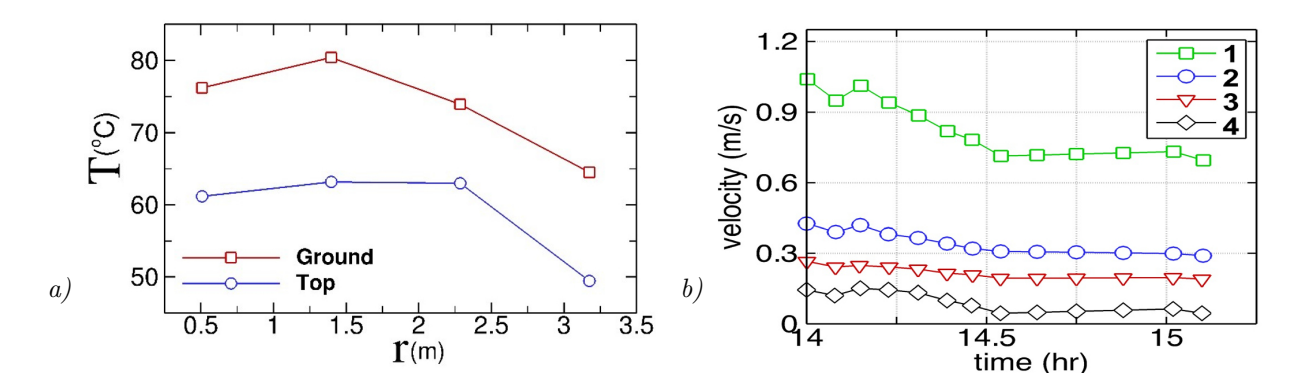


Figure 3. a) Time-averaged temperature records at the ground and collector cover, and b) estimated radial velocity at various radial locations (Figures reproduced from Ladan et al.<sup>20</sup>).

311.55K. The reference air density,  $\rho_a = \rho_{ref} = 1.132 kgm^{-3}$ , and the density of the air inside the chimney,  $\rho_{ch} = 1.035 kgm^{-3}$  were calculated from the ideal gas equation. The chimney updraft velocity,  $v_{ch}$ , obtained from the difference in pressure between chimney base and surroundings,

$$\Delta p = \rho_a g H_{ch} \frac{\Delta T}{T_a} = \frac{1}{2} \rho_a v_{ch}^2 \,, \tag{14}$$

was approximately  $3.28ms^{-1}$ . A control volume analysis between collector inflow and chimney outflow,

$$\rho_a 2\pi r_1 h v_{in} = \rho_{ch} \pi r_{ch}^2 v_{ch} , \qquad (15)$$

was used to calculate the collector inflow bulk velocity,  $v_{in} = 0.124ms^{-1}$ . From this the reference velocity,  $u_{ref} = u_{max} = (3/2)v_{in}$  was obtained. The reference Reynolds number and Rayleigh number were found to be approximately 365.90 and 704,072, respectively.

#### B. Numerical Analysis

According to the radial continuity equation, the velocity in inward radial channel flow increases almost hyperbolically (Fig. 4)in the streamwise direction. Previous numerical investigations with random steady inflow forcing<sup>22,23</sup> suggested that the stability of inward radial RBP flow is quite different from the stability of plane RBP flow. Because of the stabilizing effect of the streamwise acceleration, the inward radial RBP flow is expected to be less unstable than the plane RBP flow.

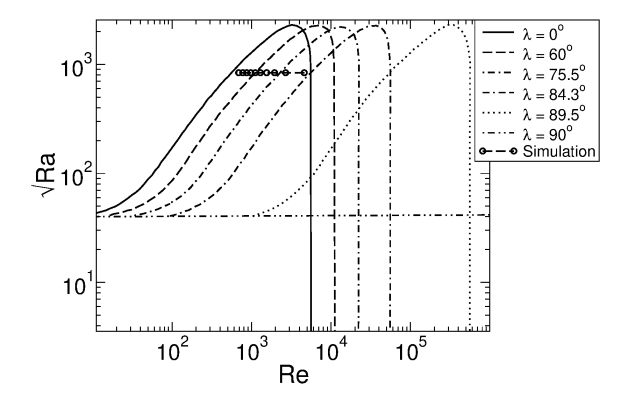


Figure 4. Conditions for present simulation indicated by the symbols in stability diagram by Gage and Reid.<sup>5</sup>

As the flow accelerates, the local Reynolds number increases above the inflow Reynolds number, Re = 365.90 and the Rayleigh number on the other hand remains constant, Ra = 704,071.57. The local Reynolds

and Rayleigh number for the present simulation were included in the stability diagram by Gage and Reid<sup>5</sup> (Fig. 4). According to Gage and Reid,<sup>5</sup> for  $Re < Re_c = 5400$  and  $Ra > Ra_c = 1708$ , 3-D waves with a wave angle of 90 degrees are most amplified. At the inflow the Rayleigh number is almost high enough for 2-D waves with a wave angle of 0 deg to be amplified. As the flow accelerates and the Reynolds number increases, the range of wave angles for unstable oblique waves becomes increasingly more narrow (e.g.  $\lambda > 60$  for  $Re \approx 1000$  and  $\lambda > 84.3$  for  $Re \approx 5000$ ).

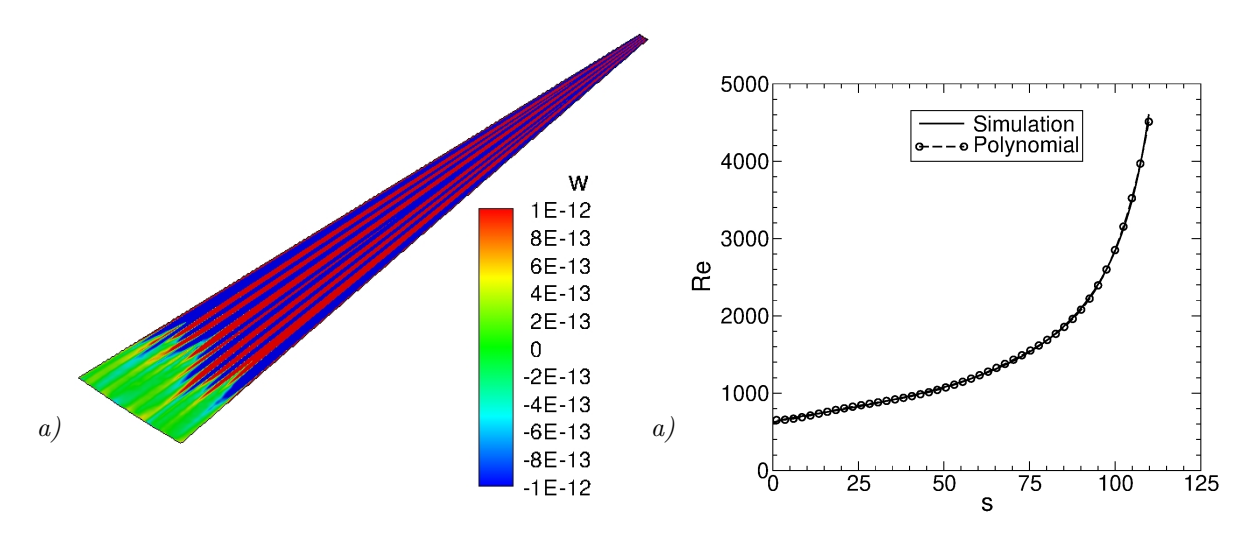


Figure 5. a) Contours of azimuthal velocity at mid-channel height, and b) local Reynolds number versus streamwise coordinate.

For the investigated case, a 3-D basic flow (no disturbance) was computed first. Unsteady randomized disturbances for all three velocity components with a maximum amplitude of  $10^{-6}$  were then added to the basic flow at the inflow boundary to excite a broad spectrum of frequencies and a wide range of streamwise and azimuthal wavelengths. The simulation was then advanced in time until all disturbance waves had reached the outflow boundary. Instantaneous azimuthal velocity contours in Fig. 5a reveal steady 3-D waves. Unlike for plane RBP flow, as the disturbance waves travel downstream, they appear to merge. This can be explained by the fact that only integer multiples of the spanwise wavelength are possible for a given azimuthal extent. In Fig. 5b the local Reynolds number is plotted versus the streamwise coordinate. The inflow boundary is at s=0 and the outflow boundary is at s=115. According to Fig. 5b, the local Reynolds number behaves almost hyperbolically in the radial direction which confirms the strong streamwise acceleration. Because of the radial acceleration, the instability associated with inward radial RBP flow is expected to be different than that of plane RBP flow.

The simulation data obtained from the present DNS were Fourier transformed in time and then Fourier transformed in the azimuthal direction. From this double Fourier transformed data, the growth rates, wave angles and phase speeds were computed. According to Gage and Reid,<sup>5</sup> in addition to the most amplified 3-D steady waves, oblique waves can also be amplified in buoyancy-driven plane RBP flow. It is therefore very interesting to see if the oblique modes are also amplified for radial RBP flow. Figure 6 exhibits contours of the spatial growth rate,  $\alpha_i$  versus frequency,  $\omega$  and azimuthal wavenumber,  $\beta$ , for three different streamwise locations (s = 57.5, 71.875, and 86.25). The total non-dimensional simulation time was T = 512 which sets the lowest frequency,  $\omega = 2\pi/T = 0.0122$ . Since data were output every  $\Delta T = 0.15$ , the highest frequency (Nyquist frequency) was  $\omega = \pi/\Delta T = 20.944$ . The growth rates for  $\omega > 10$  are very noisy, likely because the temporal resolution of the output was too low. The plus sign (" $+\beta$ ") indicates right-traveling waves and the minus sign ("- $\beta$ ") indicates left-traveling waves. From Figs. 6a,b, and c it can be concluded that the steady azimuthal modes ( $\omega = 0$ ) experience the highest spatial growth rates. The growth rates of the leftand right-traveling waves are almost identical and decrease towards the higher frequencies which is also the case for plane RBP flow.<sup>29</sup> The contour plots in Figs. 6 indicate the largest spatial growth rates for steady waves with azimuthal wavenumber  $\beta \approx \pm 4.2$  for all three radial locations. Overall, the growth rates decrease in the downstream direction which can be attributed to the streamwise acceleration. This observation is in agreement with stability analyses for boundary layers which show that acceleration is stabilizing. In Fig. 7

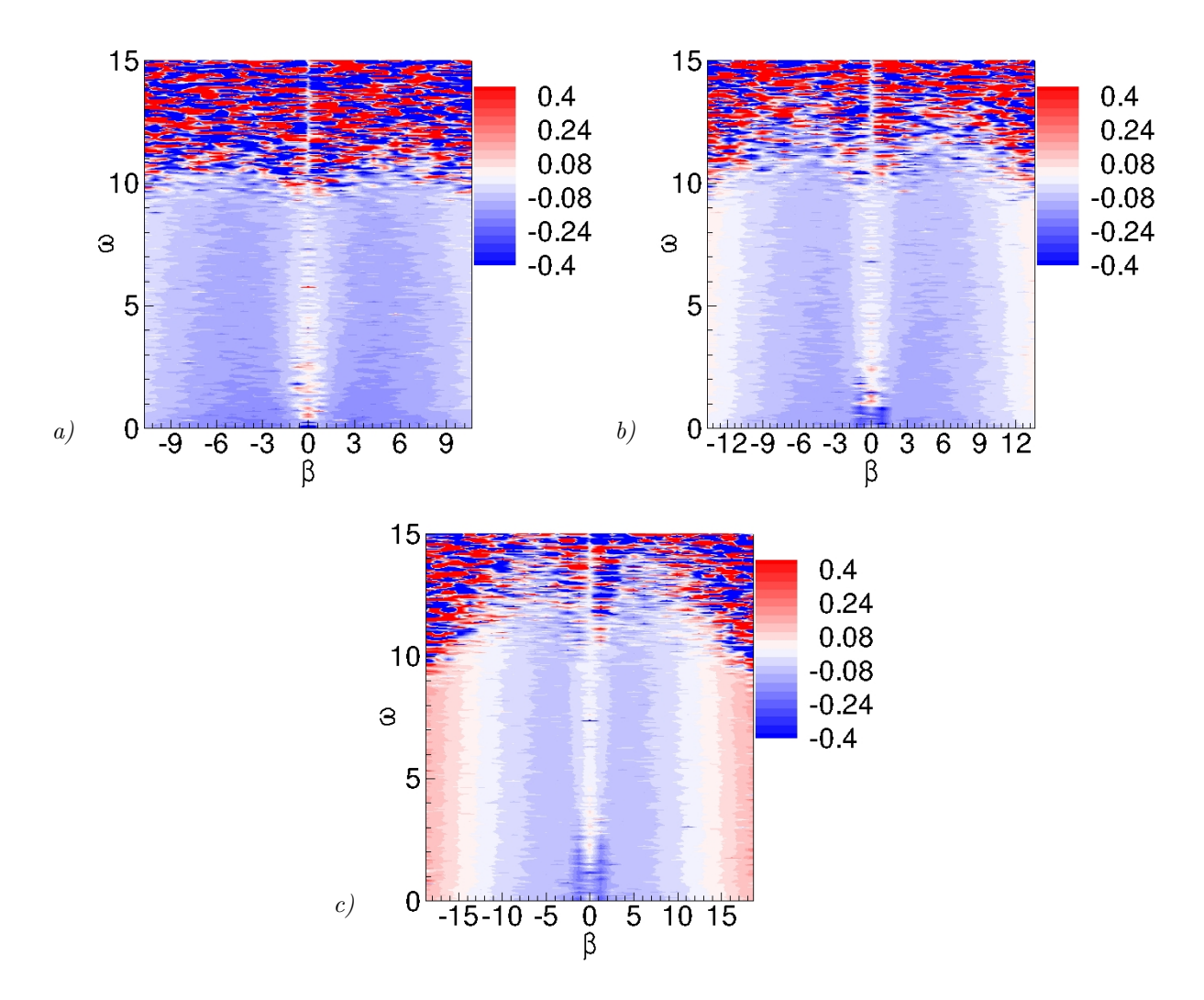


Figure 6. Contours of spatial growth rate,  $\alpha_i$ , for different frequencies and azimuthal wavenumbers for a) s = 57.5, b) s = 71.875 and c) s = 86.25.

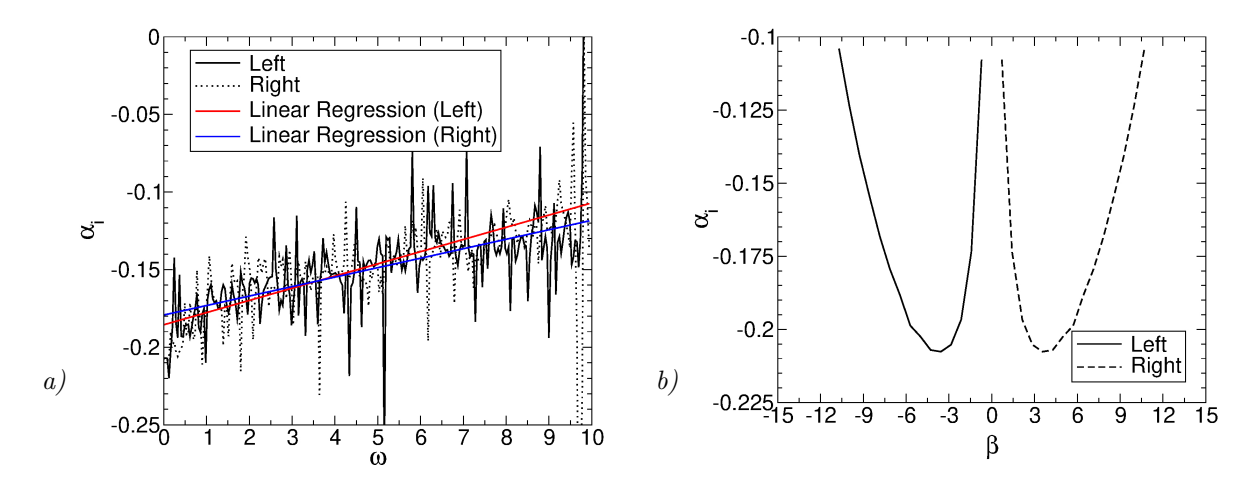


Figure 7. Spatial growth rates at s=57.5 for a)  $\beta \approx \pm 4.2$  and b)  $\omega=0$  (data extracted from Fig. 6a.)

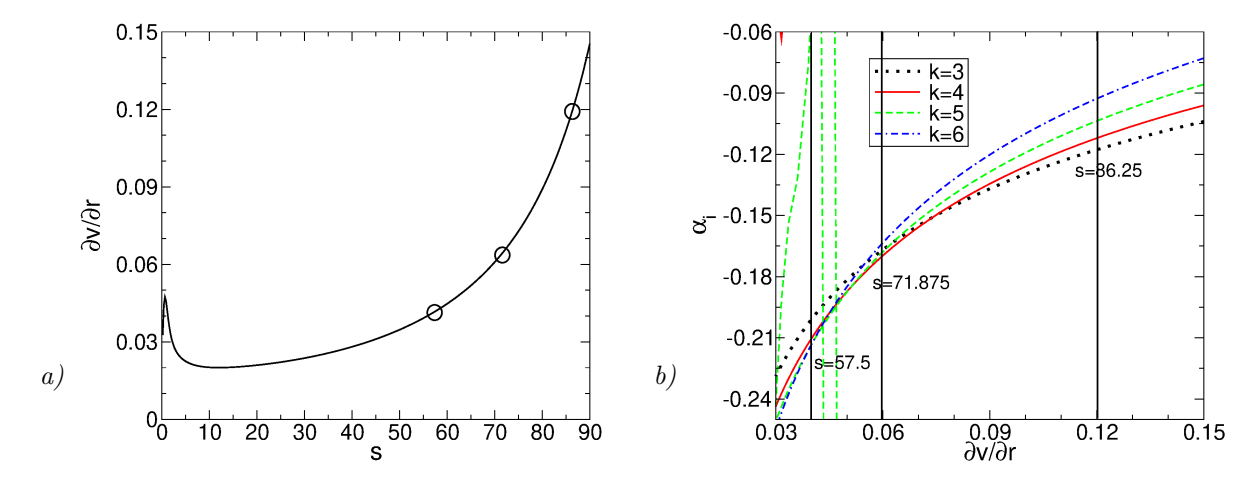


Figure 8. a) Radial acceleration versus streamwise coordinate and b) growth rates for steady modes versus radial acceleration.

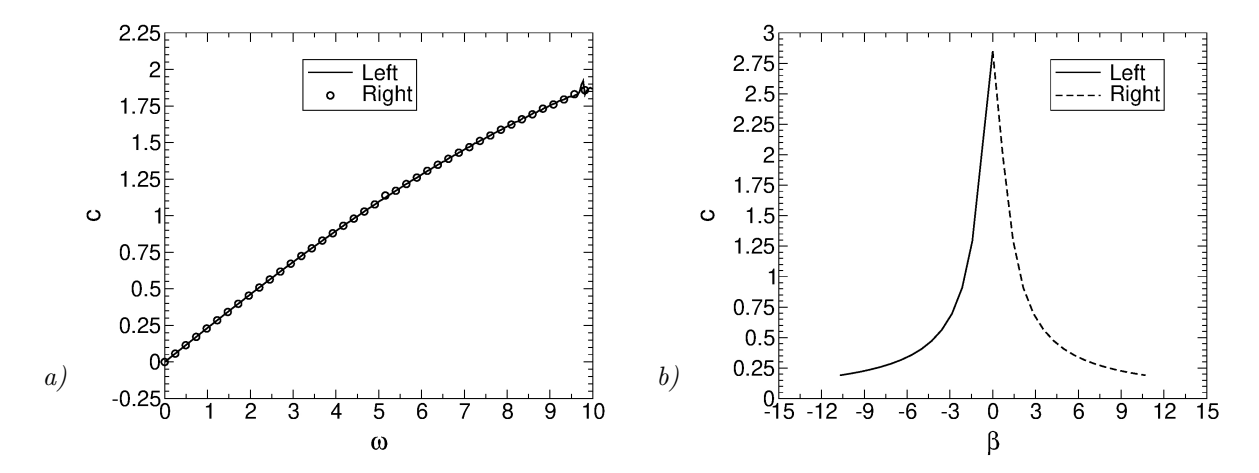


Figure 9. Phase speed versus a) frequency for fixed azimuthal wavenumber,  $\beta = 4.2$ , and b) azimuthal wavenumber for fixed frequency,  $\omega = 2.045$  (s = 57.5).

the growth rates for the most amplified azimuthal wavenumber ( $\beta \approx \pm 4.2$ ) and steady modes ( $\omega = 0$ ) are compared for s = 57.5. Figure 7a confirms that the spatial growth rates for the left and right oblique modes are almost identical and decrease with frequency. Figure 7b shows that the highest growth rate is obtained for an azimuthal wavenumber of approximately four. In Fig. 8a it is observed that the radial acceleration  $(\partial v/\partial r)$  increases in the streamwise direction. The spatial growth rates of the steady modes are plotted over the radial acceleration in Fig. 8b. The lines in Fig. 8b for three radial locations (s = 57.5, 71.875, and 86.25) correspond to the circles in Fig. 8a. Figure 8b reveals that the growth rates decrease with the radial acceleration. While the higher mode numbers such as k = 6 are more amplified upstream (e.g. s = 57.5), as the flow travels downstream, the lower azimuthal mode numbers such as k = 3 at s = 86.25 become more amplified. Nevertheless, the azimuthal wavenumber corresponding to the most amplified steady modes at the different radial locations (k = 6 at s = 57.5, k = 4 at s = 71.875, and k = 3 at s = 86.25) remains close to  $\beta \approx 4$ .

Along with the investigation of the behavior of the spatial growth rate, it is interesting to see how the phase speed depends on the frequency and azimuthal wavenumber. In Fig. 9a the phase speed of the right-and left-traveling oblique waves for  $\beta=4.2$  is graphed over the frequency for s=57.5. It is noticed that, with increasing frequency, the phase speed of both the right- and left-traveling waves increases. For the same streamwise location, in Fig. 9b the phase speed is plotted over the azimuthal wavenumber for a fixed frequency,  $\omega=2.045$ . The phase speed of the oblique waves decreases with the azimuthal wavenumber. In Fig. 10a the wave angle for  $\beta=\pm4.2$  is plotted versus the angular frequency and in Fig. 10b the wave angle

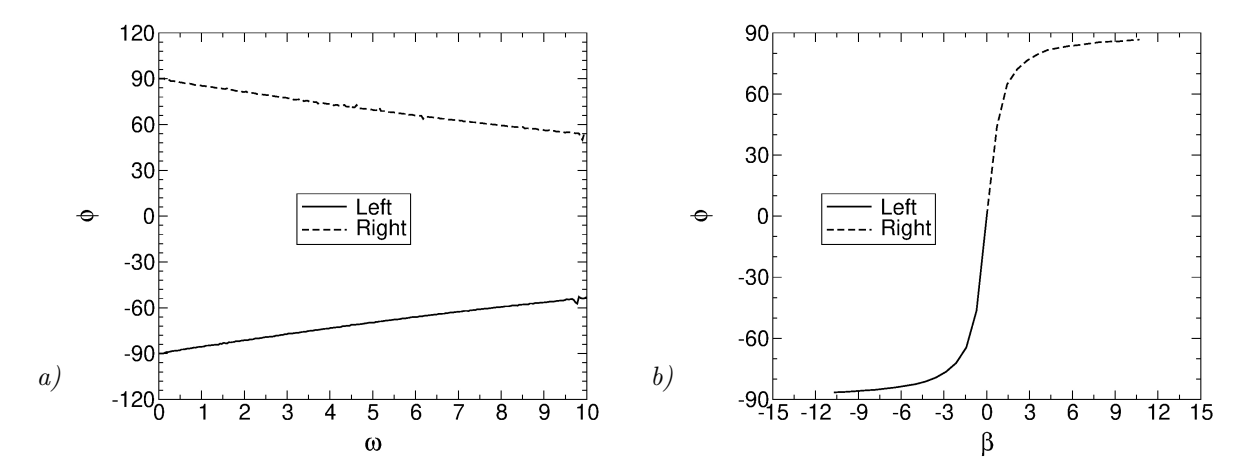


Figure 10. Wave angle versus a) frequency for fixed azimuthal wavenumber,  $\beta = 4.2$ , and b) azimuthal wavenumber for fixed frequency,  $\omega = 2.045$  (s = 57.5).

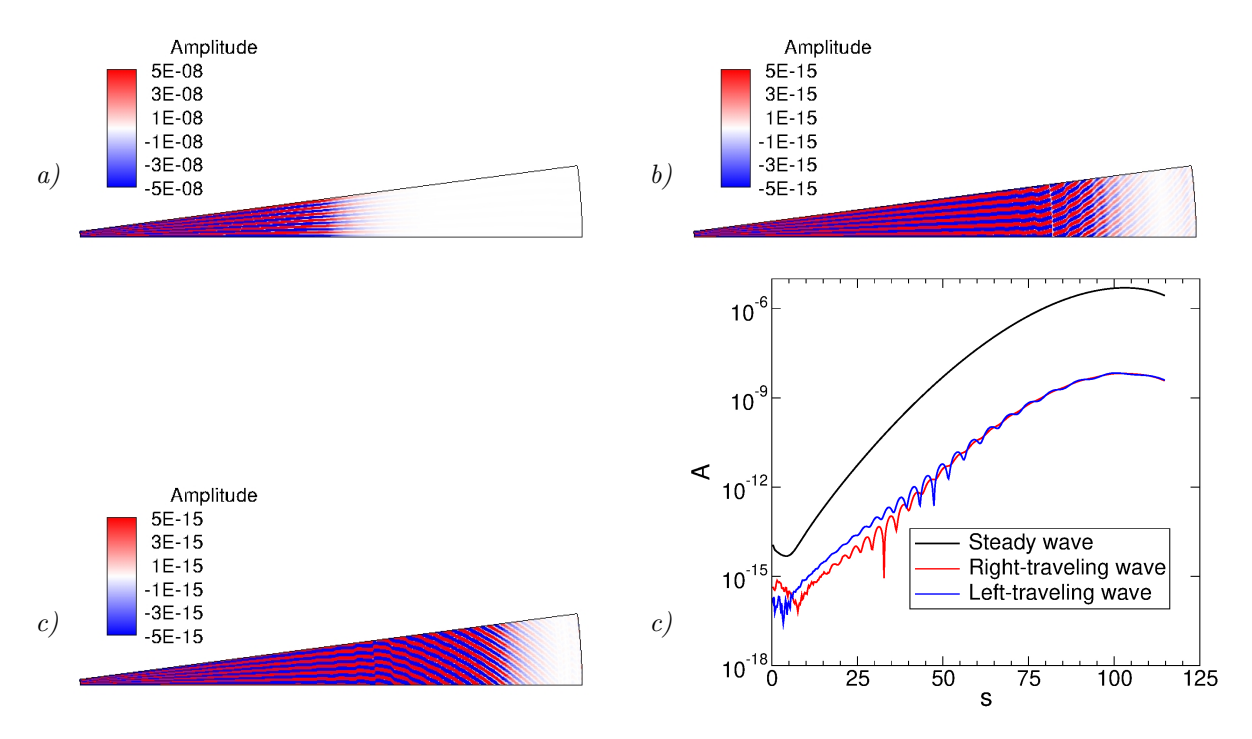


Figure 11. Iso-contours of wall-normal disturbance amplitude at channel mid-height for k=6: a) steady waves  $(\omega=0)$ , b) right traveling waves  $(\omega=4.09)$ , c) left traveling waves  $(\omega=4.09)$ . d) Mode amplitudes versus streamwise coordinate for k=6.

for  $\omega=2.045$  is plotted versus the azimuthal wavenumber. The wave angle decreases with frequency and increases with azimuthal wavenumber.

Mode shapes, reconstructed from the amplitude and phase distributions, for  $\omega = 0$  (steady) and  $\omega = 4.09$  (oblique) for azimuthal mode number k = 6 in  $r - \theta$  plane at the middle of the channel are shown in Fig. 11. The mode shape for  $\omega = 0$  (steady mode) reveals wave fronts that are aligned in the radial direction (Fig. 11a). Figures 11b and 11c illustrate that the right- and left-traveling oblique modes are symmetric with respect to each other. The wave angle of the oblique modes increases in the streamwise direction as the local Reynolds number increases. This findings is in agreement with the neutral curves by Gage and Reid.<sup>5</sup> Because of the overall higher amplification, the steady mode reaches a much larger amplitude than the oblique modes (Fig. 11d).

## Conclusions

The Rayleigh-Bénard-Poiseuille (RBP) flow inside the collector of a solar chimney power plants (SCPPs) can exhibit both buoyancy and viscosity-driven instability. For plane RBP flow, buoyancy-driven instability occurs and 3-D waves are most unstable for  $Re < Re_c = 5,400$  and  $Ra > Ra_c = 1,708$ ,. On the other hand, viscosity-driven instability leads to the growth of Tollmien-Schlichting waves for  $Re > Re_c$  and  $Ra < Ra_c$ . Despite the fact that plane RBP flow has attracted a lot of attention in the literature, the hydrodynamic instability of inward radial channel flows with vertical temperature gradient (i.e. collector of SCPP) has not been investigated much.

An instrumented scaled SCPP experiment by Ladan et al.<sup>20</sup> provided the boundary conditions and geometric dimensions for the present direct numerical simulation of the flow through a collector. Random noises was introduced at the inflow boundary and the downstream development of the disturbance waves was investigated. Three-dimensional steady waves were found to be the most amplified in the streamwise direction. The azimuthal wavenumber remains nearly constant in the streamwise direction. Mass conservation demands that the radial velocity increases almost hyperbolically in the streamwise direction. As a result of the strong streamwise acceleration, as the flow approaches the outflow, the growth rates sharply decrease. In agreement with Gage and Reid,<sup>5</sup> the analysis also revealed amplified traveling oblique waves. The growth rates of the traveling waves decrease with increasing frequency. The phase speeds increase and the wave angles decrease with frequency. Because of the stabilizing effect of the flow acceleration and the low initial amplitude which are typical of the outdoor environment, the disturbance amplitudes never get large enough to be measurable above the background noise.

# Acknowledgments

This material is based upon work supported by the National Science Foundation under grant no. 1510179 with Dr. Ronald Joslin serving as program manager.

## References

<sup>1</sup>Schlaich, J., "The Solar Chimney Electricity from the Sun," Eds. F.W. Schubert and J. Schlaich, Edition Axel Menges, 1995, Deutsche Verlagsanstalt, Stuttgart, 1994, C. Maurer, Geislingen, Germany

<sup>2</sup>Haaf, W., Friedrich, K., Mayr, G., and Schlaich, J., "Solar chimneys, part I: principle and construction of the pilot plant in Manzanares," *International Journal of Sustainable Energy*, Vol. 2, No. 1, 1983, pp. 3-22

<sup>3</sup>Haaf, W., "Solar chimneys, part II: preliminary test results from the Manzanares pilot plant," *International Journal of Solar Energy*, Vol. 2, 1984, pp. 141-161

<sup>4</sup>Schlaich, J., Bergermann, R., Schiel, W., and Weinerbe, G., "Design of commercial solar updraft tower systems-utilization of solar induced convective flows for power generation," *Journal of Solar Energy Engineering*, Vol. 127, 2005, pp. 117-124

<sup>5</sup>Gage, K.S., and Reid, W.H., "The stability of thermally stratified plane Poiseuille flow," *Journal of Fluid Mechanics*, Vol. 33, part I, 1968, pp. 21-32

<sup>6</sup>Pearlstein , A.J., "On the two-dimensionality of the critical disturbances for stratified viscous plane parallel shear flows," *Physics of Fluids*, Vol. 28, No. 2, 1985, pp. 751-753

<sup>7</sup>Chang, M.Y., Yu, C.H. and Lin, T.F., "Changes of longitudinal vortex roll structure in a mixed convective air flow through a horizontal plane channel: an experimental study" *International Journal of Heat and Mass Transfer*, Vol. 40, No. 2, 1997, pp. 347-363

<sup>8</sup>Chang, M.Y., and Lin, T.F., "Experimental study of aspect ratio effects on longitudinal vortex flow in mixed convection of air in a horizontal rectangular duct" *International Journal of Heat and Mass Transfer*, Vol. 41, No. 4-5, 1998, pp. 719-733

<sup>9</sup>Luijkx, J.M., Platten, J.K. and Legros, J.C., "On the existence of thermoconvective rolls, transverse to a superimposed mean Poiseuille flow" *International Journal of Heat and Mass Transfer*, Vol. 24, No. 7, 1981, pp. 1287-1291

<sup>10</sup>Ouazzani, M.T., Platten, J.K., and Mojtabi, A., "Etude expérimentale de la convection mixte entre deux plans horizontaux températures différentes-II" *International Journal of Heat and Mass Transfer*, Vol. 33, No. 2, 1990, pp. 1417-1427

<sup>11</sup>Reed, H.L., and Saric, W.S., "Linear stability theory applied to boundary layers," Annual Review of Fluid Mechanics, Vol. 28, 1996, pp. 389-428

<sup>12</sup>Bernardes, M.A.D.S., Valle, R.M, and Cortez, M.F.B., "Numerical analysis of natural laminar convection in a radial solar heater," *International Journal of Thermal Sciences*, Vol. 38, No. 1, 1999, pp. 42-50

<sup>13</sup>Pastohr, H., Kornadt, O., and Gurlebeck, K., "Numerical and analytical calculations of the temperature and flow field in the upwind power plant," *International Journal of Energy Research*, Vol. 28, No. 6, 2004, pp. 495-510

<sup>14</sup>Xu, G., Ming, T., Pan, Y., Meng, F., and Zhou, C., "Numerical analysis on the performance of solar chimney power plant system," *Energy Conversion and Management*, Vol. 52, No. 2, 2011, pp. 876-883

<sup>15</sup>Hu, S., Leung, D.Y.C., and Chan, J.C.Y., "Impact of the geometry of divergent chimneys on the power output of a solar chimney power plant," *Energy*, Vol. 120, 2017, pp. 1-11

- <sup>16</sup>Van Santen, H., Kleijn, C.R., and Van Den Akker, H.E.A., "Mixed convection in radial flow between horizontal plates-I. Numerical simulations," *International Journal of Heat and Mass Transfer*, Vol. 43, No. 9, 2000, pp. 1523-1535
- <sup>17</sup>Van Santen, H., Kleijn, C.R., and Van Den Akker, H.E.A., "Mixed convection in radial flow between horizontal plates-II. Experiments," *International Journal of Heat and Mass Transfer*, Vol. 43, No. 9, 2000, pp. 1537-1546
- <sup>18</sup>Fasel, H., Meng, F., Shams, E., and Gross, A., "CFD analysis for solar chimney power plants," Solar Energy, Vol. 98, Part A, 2013, pp. 12-22
- <sup>19</sup>Fasel, H.F., Meng, F., and Gross, A., "Numerical and Experimental Investigation of 1:33 Scale Solar Chimney Power Plant," 11th International Conference on Heat Transfer, Fluid Mechanics, and Thermodynamics, South Africa, 20-23 July 2015. URI: http://hdl.handle.net/2263/55874
- <sup>20</sup>Bahrainirad, L., Hasan, M.K., Fasel, H.F., and Gross, A., "Experimental and numerical investigation of a roof-scale solar chimney," AIAA-Paper AIAA 2020-0838, 2020
- <sup>21</sup>Sandberg, R.D., "Governing equations for a new compressible Navier-Stokes solver in general cylindrical coordinates," *Technical Report AFM-07/07*, University of Southampton, 2007. URI: http://www.eprints.soton.ac.uk/49523/
- <sup>22</sup>Hasan, M.K., and Gross, A., "Numerical investigation of hydrodynamic stability of inward radial Rayleigh-Bénard-Poiseuille flow," AIAA-Paper AIAA 2018-0586, 2018
- <sup>23</sup>Hasan, M.K., and Gross, A., "Numerical stability investigation of inward radial Rayleigh-Benard-Poiseuille flow," AIAA-Paper AIAA 2020-2240, 2020
- <sup>24</sup>Fan, P., "The standard upwind compact difference schemes for incompressible flow simulations," *Journal of Computational Physics*, Vol. 322, 2016, pp. 74-112
- <sup>25</sup>Shukla, R.K., Tatineni, M., and Zhong, X., "Very high-order compact finite difference schemes on non-uniform grids for incompressible Navier-Stokes equations," *Journal of Computational Physics*, Vol. 224, No. 2, 2007, pp. 1064-1094
- <sup>26</sup>Fyfe, D.J., "Economical Evaluation of Runge-Kutta Formulae," Mathematics of Computation, Vol. 20, No. 95, 1966, pp. 392-398
- $^{27}\mathrm{Carlson},$  J.-R., "Inflow/outflow boundary conditions with application to FUN3D," NASA/TM-2011-217181, October 2011
- $^{28} {\rm Gross},$  A., and Fasel, H.F., "Characteristic Ghost Cell Boundary Condition," AIAA Journal, Vol. 45, No. 1, 2007, pp. 302-306
- <sup>29</sup>Hasan, M.K., and Gross, A., "Higher-order-accurate numerical method for temporal stability simulations of Rayleigh-Beńard-Poiseuille flows," *International Journal for Numerical Methods in Fluids*, doi:https://doi.org/10.1002/fld.4877